CHALMERS

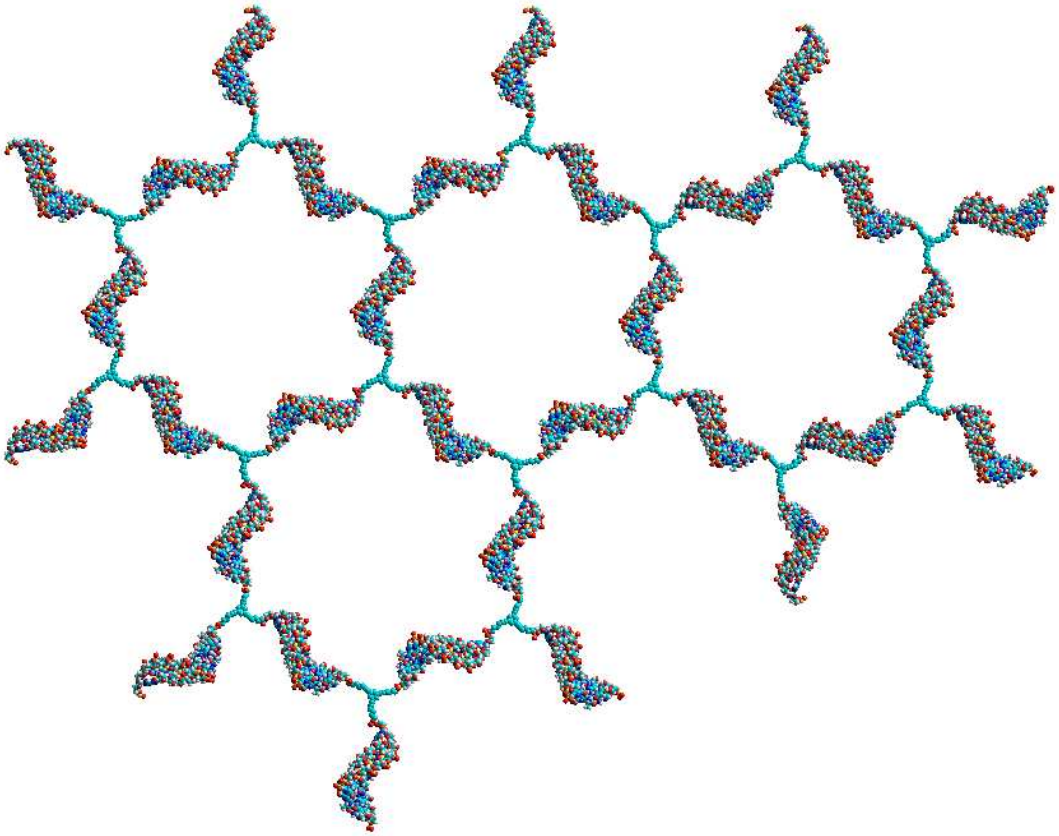

Assembly and Characterization of Two-Dimensional DNA Nanostructures Using Synthetic Three-Way Oligonucleotides

Master of Science Thesis

CALIN PLESA

Department of Chemical and Biological Engineering
Division of Physical Chemistry
CHALMERS UNIVERSITY OF TECHNOLOGY
Göteborg, Sweden, 2010

THESIS FOR THE DEGREE OF MASTER IN NANOTECHNOLOGY AND NANOSCIENCE

Assembly and Characterization of Two-Dimensional DNA Nanostructures Using Synthetic Three-Way Oligonucleotides

CALIN PLESA

This thesis was conducted under the Erasmus Mundus Master of Nanoscience and Nanotechnology with the trajectory
Technische Universiteit Delft & Universiteit Leiden (The Netherlands) and
Chalmers Tekniska Högskola (Sweden).

Division of Physical Chemistry
Department of Chemical and Biological Engineering
CHALMERS UNIVERSITY OF TECHNOLOGY
Göteborg, Sweden 2010

Assembly and Characterization of Two-Dimensional DNA Nanostructures Using Synthetic Three-Way Oligonucleotides

Calin Plesa

Technical report 12L
ISSN 0000-000X

Department of Chemical and Biological Engineering
Nordén Group

Division of Physical Chemistry
Chalmers University of Technology
SE-412 96 GÖTEBORG, Sweden
Phone: +46 (0)31-772 10 00

Author e-mail: calin@student.chalmers.se

Cover:
The four cell DNA nanostructure assembled within this project.

Assembly and Characterization of Two-Dimensional DNA Nanostructures Using Synthetic Three-Way Oligonucleotides

Calin Plesa

Division of Physical Chemistry, Chalmers University of Technology

ABSTRACT

DNA nanotechnology has gained a lot of attention due to its ability to easily self-assemble complex nanostructures. This work outlines progress towards the creation of a second generation nanometer scale non-repetitive network. This network is implemented as a large DNA nanostructure with several hexagonal unit cells composed of synthetic three-way oligonucleotides. Nodes on the network can be individually addressed through various techniques including the formation of DNA triplexes and duplexes, or using sequence-specific DNA binding proteins. This should eventually allow nanometer precision positioning of various components by attaching them to the appropriate oligonucleotide or protein and using the network as a guide. Here we focus on the characterization of these nanostructures using gel electrophoresis and atomic force microscopy.

The network is extended from a two hexagon cell structure to a four hexagon structure. Various intermediate structures as well as duplex formation between components is investigated in detail. The formation of alternative structures with yields below 5% is demonstrated. Additionally the yield of the assembly is monitored as the size of the structure is increased. A yield of 16% is found for the four hexagon cell structure, while individual duplexes have a formation yield of of 94%. The yield of the hexagonal strucutures depends primarily on the number of duplexes in the strucutre.

Keywords: DNA, bionanotechnology, nanotechnology, gel electrophoresis, AFM

Contents

List of Figures

1

Introduction

One of the fundamental goals of nanotechnology has been to be able to easily and precisely position objects on the nanometer scale. The work presented in this project is another step towards this eventual goal. The approach taken involves the creation of a DNA grid in which parts can be attached at any point on the grid to create a non-repetitive pattern. Existing top-down approaches such as photolithography, where processes are shrunk down to create smaller and smaller features, are quickly reaching their limits. Bottom-up approaches such as DNA self-assembly involve the smart design of molecules in such a way that intermolecular forces are harnessed to create useful superstructures. Bottom-up techniques bypass the limitations affecting top-down methods and can thus be used to create significantly smaller features. These properties have resulted in a lot of attention for the field of DNA nanotechnology.

1.1 DNA

DeoxyriboNucleic Acid (DNA) is a very versatile biopolymer molecule which is used as a long term data storage medium by most living things. Its unique properties make it a potentially powerful building block on the nanoscale. The molecule can be divided into two primary parts: a hydrophilic phosphate backbone, and a sequence of hydrophobic nucleotide bases. The backbone is negatively charged and consists of alternating 2-deoxyribose sugar groups and phosphate groups. DNA molecules have a directionality. Since the nucleotides are linked together through bonds on the 3' and 5' carbon atoms of the sugar, each strand has a 3' end and a 5' end which define the directionality of the strand. In biological DNA one end of the strand terminates with a sugar group (3' end) while the other ends with a phosphate group (5' end). The four types of bases (Adenine, Thymine, Guanine, Cytosine) can be further subdivided into the pairs A & T and G & C which are complementary to each other and can link through two or three hydrogen bonds respectively. This is referred to as Watson-Crick base pairing. Each molecule is composed of two strands wrapped around each other forming a helical duplex with the bases in the interior and the backbone on the outside. The base sequence on one strand is the complementary sequence of the other anti-parallel strand. By designing different sequences and attaching the strands to other molecules of interest you now have a method to attach two molecules of interest together with very high specificity. The primary advantage with using DNA as a building material comes from the fact that the various parts can simply be mixed in an aqueous solution and the desired structures will self-assemble after the mixture is cooled down from high temperature. The binding strength of the assembly depends on the number of base pairs used in the strands. Higher proportions of G & C in the strand lead to a larger binding strength, since they have an extra hydrogen bond compared to A & T. The binding strength has a corresponding melting temperature, which is the temperature needed to break apart half of the hydrogen bonds in the structure.

The Wallace-Ikatura rule [1] can be used as a simple estimate of the melting

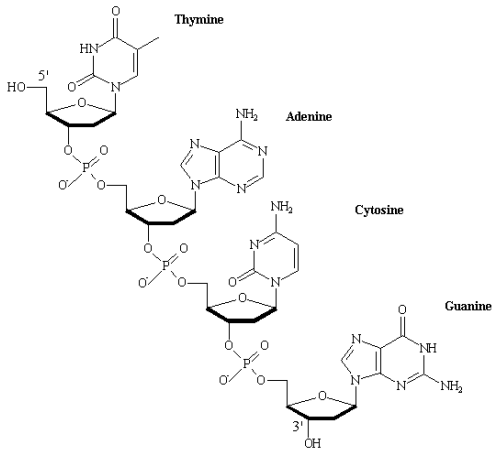

Figure 1.1: *The chemical structure of a single DNA strand, showing the nucleotides connected through the sugar-phosphate backbone.*

temperature for oligonucleotides shorter than 13 base pairs.

$$T_m = 2 * (A + T) + 4 * (G + C) \tag{1.1}$$

This simple formula does not take into account the order of the bases. A more accurate value is given by using nearest neighbor thermodynamics [2], which is available in many programs.

DNA is found in three different structural forms, although only one is commonly found in nature. This form is called B-DNA and consists of a right handed helix with a 0.34 nm spacing between the bases.

In addition to DNA duplexes, a third strand can come in and form a DNA triplex. With the appropriate sequence, a third strand will sit in the major groove of the DNA duplex and bind to the base-pairs on the interior through Hoogsteen base pairing. Although triplex sequences can be found to attach to any duplex, the binding affinities can vary greatly and the phenomenon is sensitive to pH, preferring acidic conditions [3].

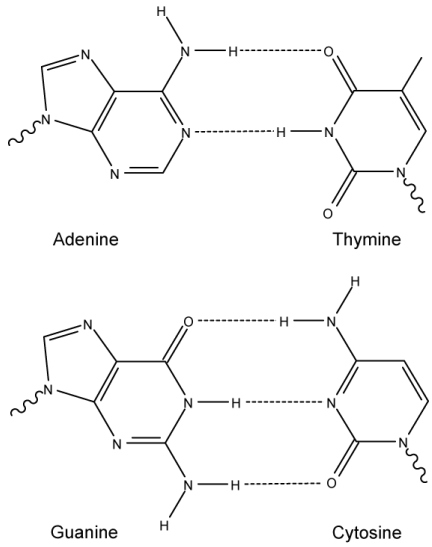

Figure 1.2: *The hydrogen bonding between the two base pairs.*

1.2 Addressable Molecular Node Assembly (AMNA)

The work in this project is based on a proposal submitted in 2005 to the EU's Sixth Framework Program, entitled Addressable Molecular Node Assembly (AMNA). This proposal envisioned the creation of a large hexagonal grid which would be digitally addressable through molecular recognition. Due to its favorable characteristics, particularly the simple self-assembly required and the resulting high structural fidelity, DNA was chosen as the building material. The key aspect of this project was that each node on the grid would have a unique address [3]. The end goal being to create a tool for experimentalists which could give them the ability to place functional groups at specified places on the grid with sub-nm level precision.

Early work in the AMNA project showed that a two-hexagon, Naphthalene like construct could be assembled. Furthermore a triplex forming oligonucleotide containing synthetic base analogues could attach itself to one of the construct's arms at low pH and be subsequently removed at higher pH [3]. The

goal of this thesis was to expand on this initial DNA nanostructure and add two more hexagonal cells to create a four cell construct.

1.3 DNA Nanotechnology

The use of DNA as a structural material has gained a lot of attention in the last two decades. In 1991 Ned Seeman unveiled a small cube with the sides made of DNA [4]. Since then many other DNA based structures have been created. The exponential drop in the cost of DNA synthesis [5] has led to an explosion of research in this area. One particularly interesting technique which is quite prevalent today is known as DNA origami. This technique, developed by Paul Rothemund [6] in 2006, involves folding a scaffold, usually the λ-phage genome, into a desired shape using short oligonucleotides designed to bring several parts of the scaffold together. This can be used to create any desired shape out of DNA. Since then more advanced structures such as nanoarrays [7] and three dimensional boxes [8] have been created using this technique. All of these developments highlight the great potential which exists in this field.

2
Theory

Two-primary methods of characterization were employed in this project, gel-electrophoresis and atomic force microscopy. This section provides some of the theoretical framework for these techniques.

2.1 Gel Electrophoresis

Gel electrophoresis is a common method used to separate charged macromolecules. The macromolecules are placed in a gel which is a porous polymer matrix. The size of the pores in the gel depends on the concentration of the polymer, usually agarose. When these molecules are then exposed to an electric field they will move towards the opposite charge. The mobility of a molecule will depend on its shape, size, and charge as shown in Figure 2.1. Due to the pores in the

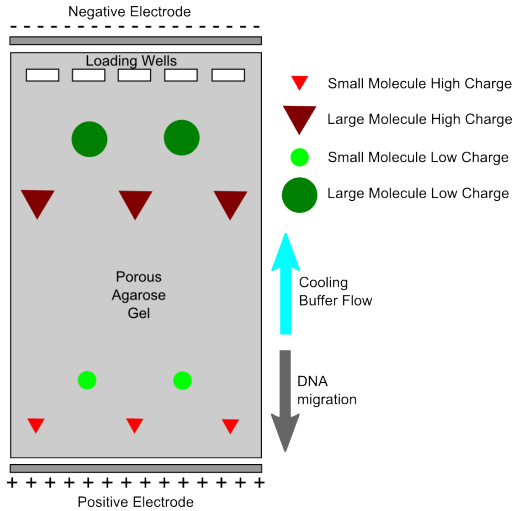

Figure 2.1: *A typical gel electrophoresis setup.*

gel, the molecule's shape plays an important part in determining its mobility. A linear molecule and a closed-ring molecule of same charge and size will travel at different rates through the gel. We can define a molecules electrophoretic mobility μ as

$$\mu = \frac{\nu}{E} = \frac{q}{f} \tag{2.1}$$

where ν is the velocity of the molecule, E is the electric field, q is the charge, and f is the coefficient of friction. In this equation the friction term dominates when dealing with DNA. This means that the length of the sequence will be more important than the charge of the molecule.

Several models exist to describe the behavior of the molecules in the gel. The Ogston model [9, 10] is best suited to describe behavior for the conditions encountered in this project. This model describes the mobility of short DNA molecules (<10 kbp) in low electric fields. This condition prevents alterations in the conformation of the DNA molecules. According to the model, the distribution of the volume fraction of pores large enough to contain a molecule of

size R_g is given by

$$P(R_g) = e^{-\pi\nu l(r+r_g)^2} \tag{2.2}$$

where r is the radius of the gel fibers and ν is the average number of fibers per unit volume. Together with the assumption that the volume fraction of the pores is proportional to the electrophoretic mobility $\mu \propto P(R_g)$, the electrophoretic mobility is related to the molecule size (R_g) and pore size (R_P) by

$$\frac{\mu}{\mu_0} = e^{-\frac{\pi}{4}(\frac{R_g}{R_P})^2} \tag{2.3}$$

where μ_0 is the mobility in free solution [11].

2.2 AFM

An Atomic Force Microscope (AFM) is a type of microscope which can be used to investigate nanoscale features on surfaces. The microscope consists of a probe which is scanned across the surface of a sample. The probe is an atomically sharp tip on the end of a cantilever. As the tip is brought close to the surface of the sample, interaction forces including van der Waals, electrostatic, and capillary cause a deflection in the cantilever. This deflection is measured by reflecting a laser beam off the back of the cantilever and passing it through an optical lever into a multisegment photodiode. Cantilever deflections are measured as a differential current between the segments of the photodiode. By recording the change in the current of the photodiode relative to the tips position on the sample, the topology of the surface can be determined. The basic setup is illustrated in Figure 2.2. Several different operating modes exist which can be described based on their regions of operation in the tip-sample interaction potential shown in Figure 2.3. In contact mode, the tip is touching the sample and repulsive forces dominate. In this mode the tip is essentially being dragged across the surface of the sample. Due to the high forces involved, damage to the sample and tip can occur. The tip also loses its sharpness much more quickly.

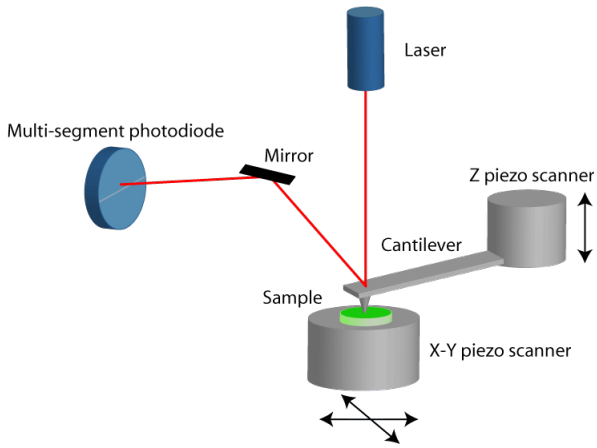

Figure 2.2: *The basic system layout of an Atomic Force Microscope.*

Semi-contact mode operates in the attractive region of the potential. In this region, where the separation distances are on the order of a few nanometers, the attractive van der Waals force dominates. Here the tip is vibrated and only enters the attractive part of the potential for a brief time at one end of its periodic motion. Unlike in contact mode, semi-contact avoids effects cause by frictional and adhesive forces. Since the samples being investigated are soft matter, the

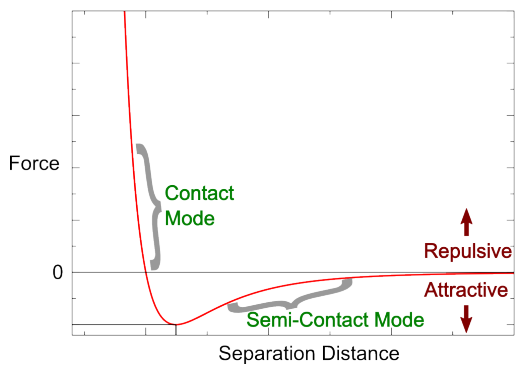

Figure 2.3: *The tip-sample interaction potential, showing different operating modes.*

semi-contact imaging mode is used. The tip is vibrated at its resonance frequency and as it begins to feel the surface, the interaction causes a reduction in its resonance frequency. This reduction is measured and used to determine the tip-sample separation distance. The resonance frequency of the cantilever is given by

$$\omega = \sqrt{\frac{k}{m}} \tag{2.4}$$

where k is the spring constant and m is its mass. For the AFM cantilevers used in this project the spring constant is given by beam theory [12] as

$$k = \frac{3EI}{L^3} \tag{2.5}$$

where I is the moment of inertia, E is Young's modulus, and L is the length of the cantilever. In vacuum the resonance frequency of the cantilever becomes

$$f_v = \left(\frac{\alpha_i}{L}\right)^2 \sqrt{\frac{EI}{\rho A}} \tag{2.6}$$

where α_i is a constant for the resonance mode, and A is the cantilever's cross sectional area [13]. When operated in air, the resonance frequency is reduced by a few percent. Once the tip encounters the attractive potential of the surface an additional interaction term is added to the spring constant of the cantilever $k_{new} = k_{cantilever} + k_{interaction}$, which drops the resonance frequency.

Since the tip is much larger than the separation distance, we need to look at the interaction of every atom in the tip with the surface below in order to determine the interaction potential. If we model the tip as a sphere of radius R, a distance d above a flat surface, and integrate the forces between the atoms in the tip and surface, a good estimate for the potential can be made.

$$U = -\frac{AR}{6}\frac{1}{d} \tag{2.7}$$

where A is the Hamaker constant defined by

$$A = \pi^2 C \rho_1 \rho_2 \tag{2.8}$$

with C being the interaction constant of the van der Waals potential and ρ the material densities of the tip and sample respectively.

3

Materials and Methods

In the work which led up to this project, two different implementation routes were used [14]. The first consisted of using long 22 base pair oligonucleotides to form the hexagon structures. Here the leading and ending 10 base pair regions would form duplexes with other oligonucleotides, while two Thymine bases in-between would act as a hinge.

The secondary route, which is the focus of this thesis, involves a three way node structure shown in Figure 3.1. Here three 10 base pair oligonucleotides are attached covalently to the 1,3,5-trihex-1-ynylbenzene node. By using different protection groups on each arm, three different oligonucleotides can be attached through either their 3' or 5' end to the central node. For each node two oligonucleotides were attached through their 3' ends and the third through its 5' end. All synthesis work was performed by project collaborators at the

University of Southampton. An assembly of six nodes can be used to form a

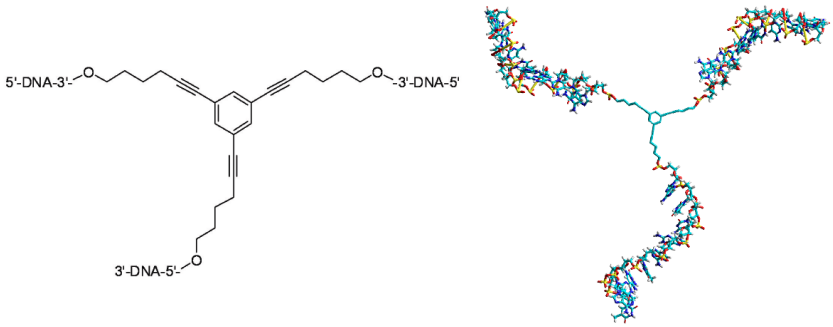

Figure 3.1: *The Lewis structure of the three way node and a full node with attached oligonucleotides.*

hexagon unit cell as shown in Figure 3.2.

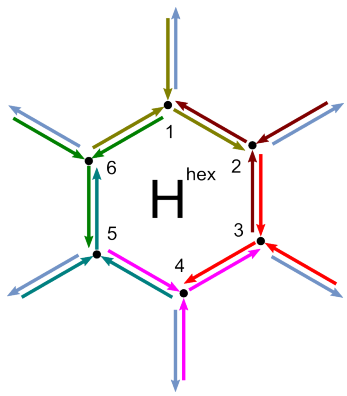

Figure 3.2: *Six nodes forming a hexagon unit cell.*

The full DNA structure to be assembled is shown in Figure 3.3. Each of the nodes was given a unique name H^{hex}, N^{hex}, A^{hex}, and P^{hex} derived from Hexagon, Naphthalene, Anthracene, and Phenalene respectively due to the sequence in which the structure was to be assembled. Work completed and published before this project had verified the successful formation of the Naph-

thalene like assembly formed from the H^{hex} and N^{hex} unit cells [3]. Each of the 16 different nodes used in this project have a unique sequence on each of their three branches. The complementary sequences for each arm are placed on a different node such that the fully assembled structure forms a hexagonal grid. For each of the outer arms of the assembled structure, complementary oligonucleotides were synthesized. These were synthesized both with and without fluorophores covalently attached. The fluorophores allow the assembled structures to be easily visualized during gel electrophoresis characterizations. Additionally the final structure utilized the same node (12) in two different positions as shown in Figure 3.3. The reuse of nodes could be useful if the super-structure is to be expanded even further. Since two pairs of identical duplexes were now present in the mixture, these nodes could potentially interfere with each other.

3.1 Cooling

The oligonucleotides used in this project are only 10 bases long. This allows the nodes in the grid to be very close together but results in a duplex with a very low melting temperature of about 30°. This requires the assembled products to be kept at low temperatures after hybridization. All test tubes and pipette tips are pre-cooled in a freezer before coming into contact with the samples. The gel electrophoresis setup is cooled by pumping the Phosphate buffer through tubes passing through a cooling unit with a mixture of water and glycerol kept at -6°C. The flow of the buffer is in the direction opposite to that in which the DNA is moving. This allows temperatures in the gel to be maintained in the 2 - 8°C range. In other work related to this project it has been shown that the components of the assembly can be covalently attached together [15, 16] after hybridization in order to bypass some of these temperature issues.

3.2 DNA Preparation

Standard 2 μM +/- 0.05 μM solutions of each of the nodes and complementary oligonucleotides were made by measuring the absorption at 260 nm using the

Cary 4000 spectrophotometer and using previously calculated extinction coefficients, to find the concentration. This was adjusted using standard dilution procedures until the concentration was in the proper range of values.

3.2.1 Hybridization

In order to assemble the DNA structures, 1.5 μL from each of the individual components' 2 μM stock solution was mixed together. This mixture was vortexed and placed into a heating block and kept at 90°C for 5 min, after which it was allowed to cool down to room temperature overnight (16 hours). The following morning the mixtures were placed into a 4°C fridge. After this point the temperature of the samples was not allowed to rise above 10°C.

3.3 Gel Electrophoresis

The gels used in this project were 4.5% MetaPhor Agarose by weight in Phosphate buffer. These were prepared by heating up the mixture to 150°C while stirring at 600 RPM. Once the Agarose was fully melted the heater was reduced to 50°C and the stirring to around 60 RPM, until most bubbles had been removed. Any loss due to evaporation was replenished with heated and filtered DI water. Once the gels were cast, each of the wells was individually cleaned to remove any unwanted debris and placed into the cold buffer for at least 30 min.

Since different amounts of components were used in each sample the concentration of the fluorophore in each sample was calculated. In preparing mixtures for the gel, 10 μL of the sample with the lowest fluorophore concentration was mixed with 2 μL of FICOLL loading buffer. Volumes for the remaining samples were chosen using the fluorophore concentrations such that each well would have equal amounts of the fluorophore. These mixtures were then loaded once the gel was at the correct temperature. Pumping was stopped during loading and the samples were driven in for 5 minutes before the pumping was resumed. Gels were run for 4 to 5.5 hours with a field strength of around 3 - 4 V/cm, and the electrode voltage kept at 67 V for small (40 g) gels and 60 V for

large (75 g) gels. In large gels the amount of buffer had to be carefully controlled in order to prevent the 400 mA current limit from being reached. With the electrodes' voltage at a potential of 60 V, the buffer should just be covering the top of the gel.

Upon completion, gels were scanned with a GE Typhoon 9410 Variable Mode Scanner using 100 μm per pixel resolution and a photomultiplier tube voltage of 600 - 800 V. The appropriate laser excitation sources and filters were selected using the dye characteristics shown in Table 3.1. Several gels were also post-stained using Syber Gold gel stain in order to confirm that the structure had formed in cases where the fluorophore containing oligonucleotide had not attached. Image analysis was done with ImageQuant TL software, which enabled both the comparison of band positions as well as the intensity measurements required to estimate the yield.

Table 3.1: *Fluorophores used in this project*

Fluorophore	Absorption (nm)	Emission (nm)	Laser	Filter
Cy3	550	570	Green (532nm)	580 BP
FAM	495	535	Blue2 (488nm)	520 BP
ROX	590	605	Green (532nm)	610 BP
Sybr Gold	495	537	Blue2 (488nm)	520 BP

3.3.1 AFM sample preparation

Several procedures [17] where tried during the course of this project. All procedures began by cleaving a mica substrate with some scotch tape. Previous literature [18, 19] has shown that $NiCl_2$ acts as a very good divalent cationic bridge between mica and DNA, although $CoCl_2$ and $ZnCl_2$ would also work well. Previous work done with $MgCl_2$ proved to be problematic.

Procedure A
- Mix: 2μL of 2μM DNA with 5μL of 10mM HEPES buffer and 15μL of 1mM $NiCl_2$

- Add to mica and incubate 10 min.
- Dry surface with N_2.

Procedure B
- Add 20μL of 10mM $NiCl_2$ to mica.
- Incubate 5 min and dry mica with N_2.
- Add 20μL of 0.5μM DNA to surface.
- Incubate 10 min and dry with N_2.
- Add 100μL MilliQ to surface and dry with N_2.

Procedure C
- Add 20μL of 10mM $NiCl_2$ to mica.
- Incubate 5 min and dry mica with N_2.
- Mix 15μL of 0.5μM DNA with 5μL of 10mM HEPES buffer and add to surface.
- Incubate 10 min and dry with N_2.

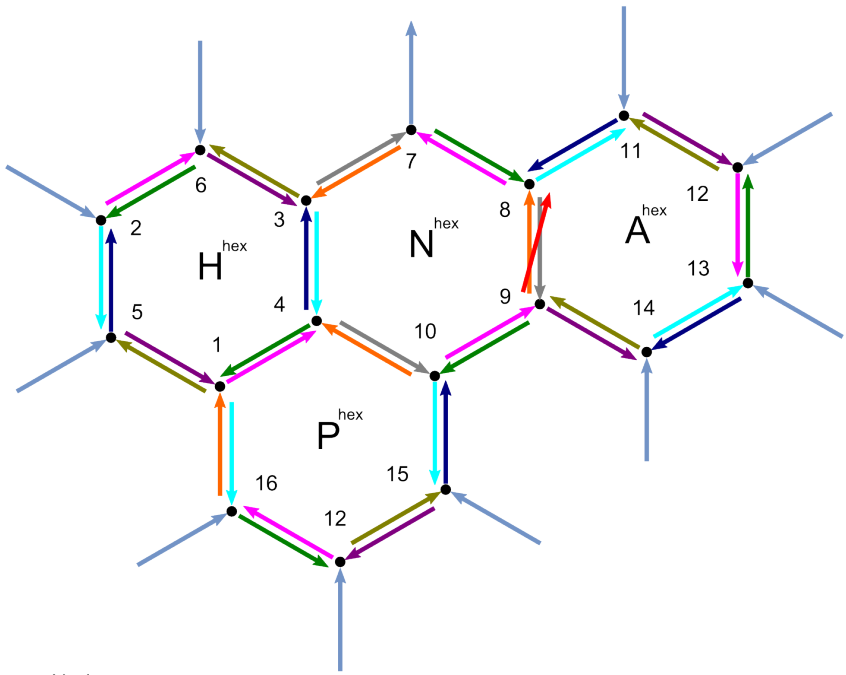

Nodes

1 5' CCATACATAC
N CCACAGCATC 3'
5' CAGCTTGAGG

2 5' GGCTCTACAG
N GAGGAGGATG 3'
5' CGGTCAAAGC

3 5' CCATACATAC
N CCACAGCATC 3'
5' CAGCTTGAGG

4 5' CCATACATAC
N CCACAGCATC 3'
5' CAGCTTGAGG

5 5' CCATACATAC
N CCACAGCATC 3'
5' CAGCTTGAGG

6 5' CCATACATAC
N CCACAGCATC 3'
5' CAGCTTGAGG

7 5' CCATACATAC
N CCACAGCATC 3'
5' CAGCTTGAGG

8 5' CCATACATAC
N CCACAGCATC 3'
5' CAGCTTGAGG

9 5' CCATACATAC
N CCACAGCATC 3'
5' CAGCTTGAGG

10 5' CCATACATAC
N CCACAGCATC 3'
5' CAGCTTGAGG

11 5' CCATACATAC
N CCACAGCATC 3'
5' CAGCTTGAGG

12 5' CCATACATAC
N CCACAGCATC 3'
5' CAGCTTGAGG

13 5' CCATACATAC
N CCACAGCATC 3'
5' CAGCTTGAGG

14 5' CCATACATAC
N CCACAGCATC 3'
5' CAGCTTGAGG

15 5' CCATACATAC
N CCACAGCATC 3'
5' CAGCTTGAGG

16 5' CCATACATAC
N CCACAGCATC 3'
5' CAGCTTGAGG

Figure 3.3: *The various nodes used to assemble the DNA nanostructure. The 5' or 3' endings of the oligos are labeled while the N represents the position of the node.*

Complementary Oligonucleotides

1*	5'	CCTCAAGCTG	3'	9*	5' CTGCTACGTG 3'
2*	5'	GCCAGTTTCG	3'	10*	5' GCCTTCATTG 3'
3*	5'	CCGTTAGGAC	3'	11*	5' GTGGTTCAGA 3'
4*	5'	ACCAGAGAGG	3'	12*	5' CGAAGTGTCT 3'
5*	5'	GTACTGCAAG	3'	13*	5' CATCTGTTCG 3'
6*	5'	CTTCTCACAC	3'	14*	5' CCGACTATGT 3'
7*	5'	AGCCAACAAG	3'	15*	5' CTGGACTCGT 3'
8*	5'	GGCGTGTAAC	3'	16*	5' CGCGACAACT 3'

Cy3 Labeled Oligonucleotides

1'	Cy3 - 5'	CCTCAAGCTG	3'	6'	Cy3 - 5'	CTTCTCACAC	3'
2'	Cy3 - 5'	GCCAGTTTCG	3'	7"	Cy3 - 5'	AGCCAACAAG	3'
3'	Cy3 - 5'	CCGTTAGGAC	3'	8"	Cy3 - 5'	GGCGTGTAAC	3'
4'	Cy3 - 5'	ACCAGAGAGG	3'	9"	Cy3 - 5'	CTGCTACGTG	3'
5'	Cy3 - 5'	GTACTGCAAG	3'	10"	Cy3 - 5'	GCCTTCATTG	3'

FAM Labeled Oligonucleotides

11'	FAM - 5'	GTGGTTCAGA	3'	11°	5'	GTGGTTCAGA	3' - FAM
12'	FAM - 5'	CGAAGTGTCT	3'	12°	5'	CGAAGTGTCT	3' - FAM
13'	FAM - 5'	CATCTGTTCG	3'	13°	5'	CATCTGTTCG	3' - FAM
14'	FAM - 5'	CCGACTATGT	3'	14°	5'	CCGACTATGT	3' - FAM

ROX Labeled Oligonucleotides

12°°	ROX - 5'	CGAAGTGTCT	3'	16°°	ROX - 5'	CGCGACAACT	3'
13°°	ROX - 5'	CATCTGTTCG	3'				

Figure 3.4: *The oligonucleotides used in this project.*

3.4 Atomic Force Microscopy

Prior to the start of AFM measurements the sample is bound to a Mica substrate as explained earlier. This substrate is placed onto the sample holder using double sided tape and a small grounding wire is brought into contact with the surface of the sample. The two tips utilized were single crystal Silicon NSG01 and NSG01/TiN tips from NT-MDT. The NSG01 probe had the following stated characteristics:

- Curvature Radius 6 nm
- Resonant Frequency (kHz) 87 to 230
- Force Constant (N/m) 1.45 to 15.1
- Length (μm) 125
- Width (μm) 30
- Thickness (μm) 2

The NSG01/TiN tip has a conductive coating and can be used to investigate the role of surface charges. These tips have similar geometry to the NSG01 tips although the coating increases the curvature radius to approximately 35 nm. These significantly reduce the lateral resolution of the device so they were not used often. When using the tips in Semi-Contact mode, the average lifetime of the tips is about 4 days. A detailed outline of the AFM startup procedure can be found in the Appendix.

The 1 μm scanner initially had a problem with the sample not being able to reach the tip because it would hit the limit of the coarse positioning system. This was addressed by cutting out a piece of glass several mm thick in the same shape as the sample holder. With this approach the glass could be placed in between the sample and the sample holder, lifting it enough that the tip could now be brought into contact. Nevertheless this approached likely modified the mechanical characteristics of the stage and a more permanent solution should be investigated.

4

Results

The following section describes the primary results of this work. The first part focuses on the verification of new structures using gel electrophoresis while the latter part looks at Atomic Force Microscope measurements.

4.1 Gel Electrophoresis

4.1.1 New Hexagon Cells

Two new hexagon cells were utilized in this work. Their proper formation was verified independently to rule out any possible interference effects present in the larger structures.

The A^{hex} hexagon shown in Figure 4.1 is integrated on the far right of the

superstructure. It was visualized in a gel, shown in Figure 4.2, by placing it in the same gel as the previously verified H^{hex} hexagon cell. The H^{hex} was labeled with Cy3 on the 2' position and can be seen in lane 6. The A^{hex} assembly can be seen in lanes 1, 2, 3, and 11 with FAM and ROX containing oligonucleotides placed on the 12' position. Based on the position of the bands we can conclude that the A^{hex} hexagon was successfully formed. The loca-

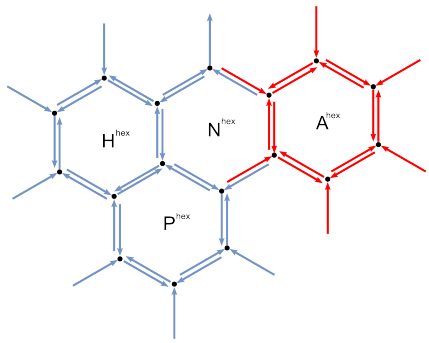

Figure 4.1: *The position of the A^{hex} hexagon cell within the larger structure.*

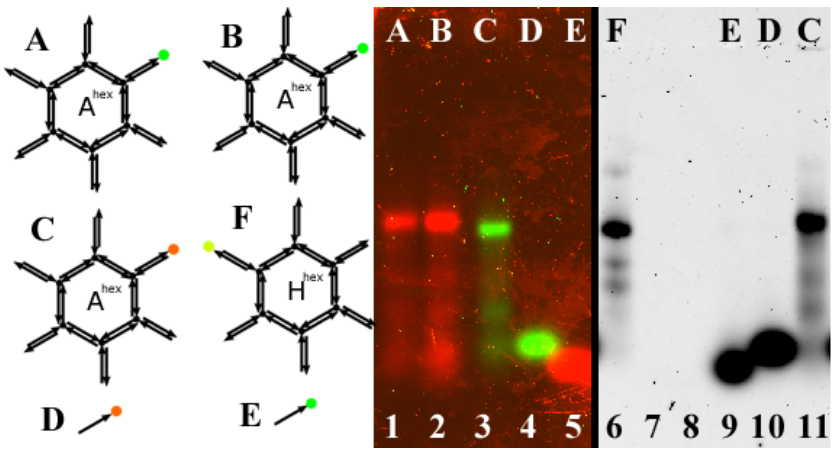

Figure 4.2: *Gel verification of the A^{hex} cell.*

tion of the second hexagon P^{hex} is shown in Figure 4.3. In a similar manner the P^{hex} was assembled and compared to H^{hex}. Figure 4.4 shows H^{hex} in

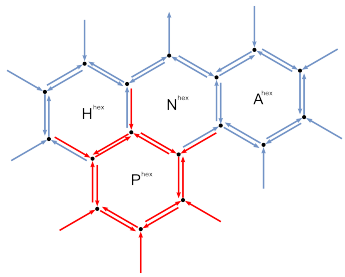

Figure 4.3: *The position of the P^{hex} hexagon cell within the larger structure.*

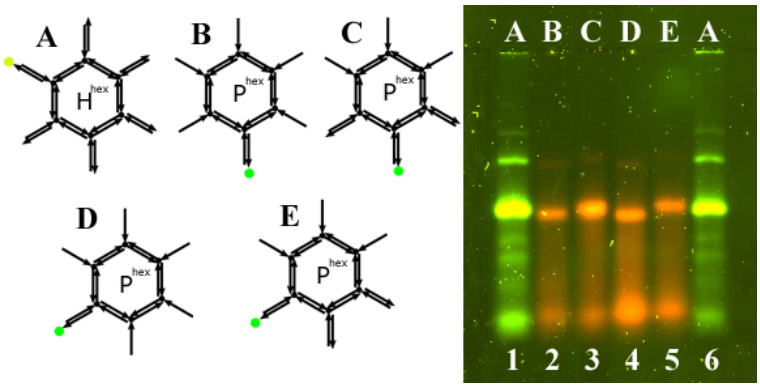

Figure 4.4: *Gel verification of the P^{hex} cell.*

the first and last lanes while P^{hex} assemblies occupy the other lanes. In this case, three of the nodes in P^{hex} did not have complementary oligonucleoties available for their outer arms so the assembly would run in the gel with three unpaired oligonucleotides. This explains the dip seen in lanes 2 and 4, which only contained the fluorophore oligo and had five unpaired strands. In lanes 3 and 5, the complementary oligos for two of the other nodes are added. The gel was run with separate lanes for constructs containing complementary oligos and those without in order to investigate possible interference effects which are

seen with this cell later on. Once again the position of the bands confirm the successful assembly of P^{hex}.

4.1.2 Step-wise build-up of Three Hexagon Assemblies

One of the primary methods used in this project to confirm the successful build-up of a new construct was step-wise build-ups in gels. In this method the first lane in the gel would consist of a previously verified structure. Subsequent lanes would contain assemblies with additional nodes, until the final construct is reached. Using this approach the first lane moves the quickest while the last lane is slowest, with the rest of the lanes in between. Figure 4.5 shows the build-up from the $H^{hex}N^{hex}$ construct in lane 1 and 8 until $H^{hex}N^{hex}A^{hex}$ in lane 7. All of the constructs in this gel contain the Cy3 fluorophore at the 2' position. Based on the position of the $H^{hex}N^{hex}A^{hex}$ band we can conclude that the full structure formed successfully.

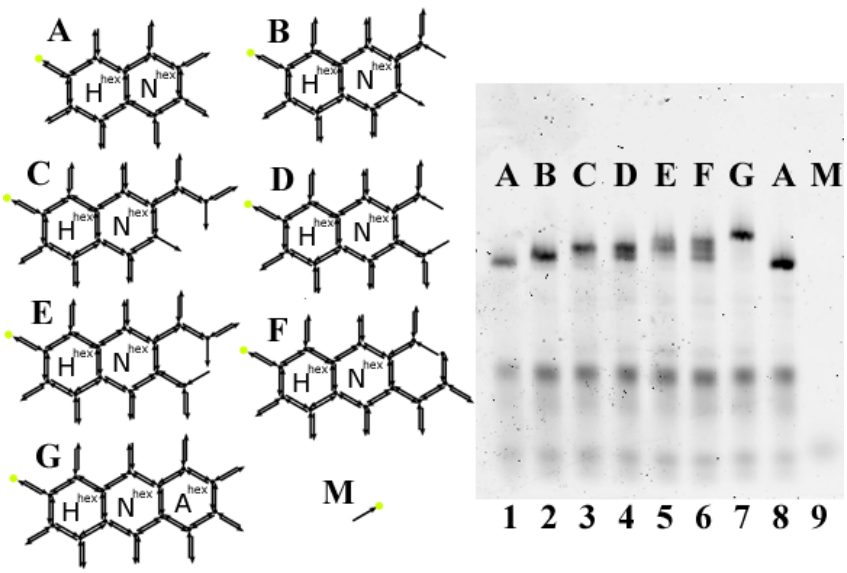

Figure 4.5: *The step-wise build-up of the $H^{hex}N^{hex}A^{hex}$ assembly.*

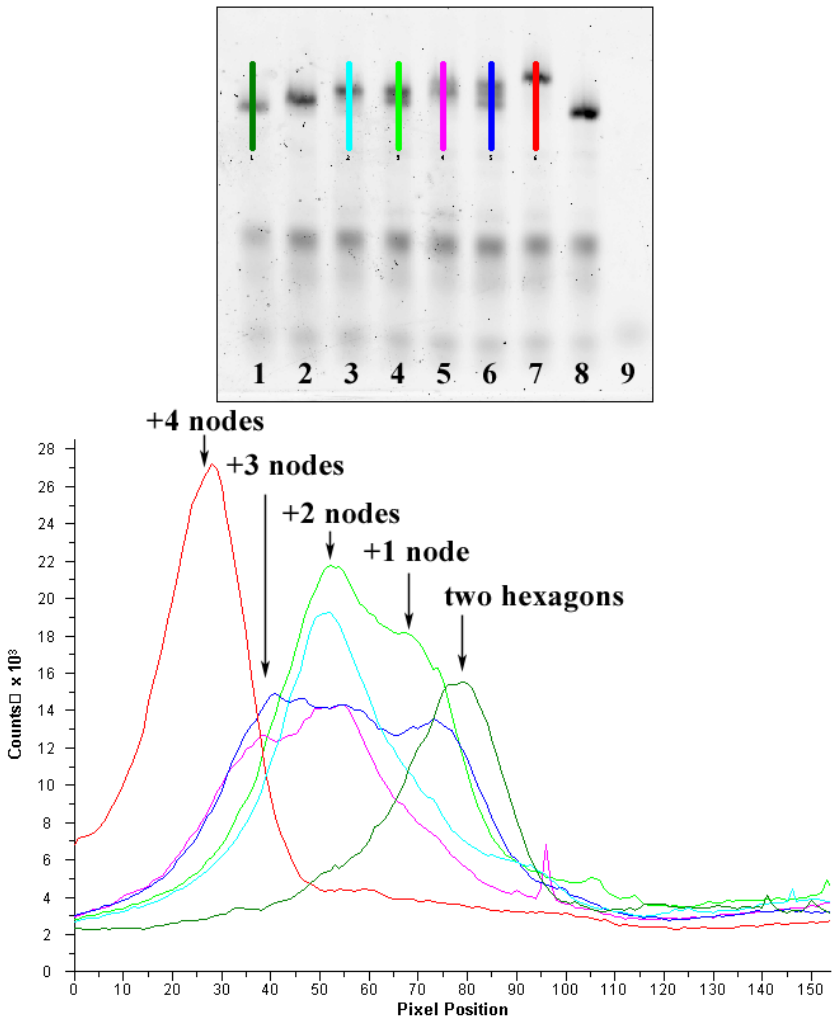

Figure 4.6: *An analysis of the multiple constructs seen in the $H^{hex}N^{hex}A^{hex}$ assembly.*

The lanes with intermediate structures often contain multiple bands. This is further analyzed in Figure 4.6. Here vertical intensity profiles are plotted against the vertical distance in pixels (100 μm/pixel) for several lanes. The intensities are averages over a horizontal area of 5 pixels in order to reduce the noise.

Both $H^{hex}N^{hex}$ in lane 1 shown in dark green as well as $H^{hex}N^{hex}A^{hex}$ in lane 7 shown in red have strong single peaks. The assembly with 2 new nodes ($H^{hex}N^{hex}A^{hex}$ + nodes 11, 12) in lane 3 which is shown in light blue also has a strong peak which defines the position for +2 node constructs. In lane 4 ($H^{hex}N^{hex}A^{hex}$ + nodes 11, 14) shown in light green, strong peaks appear for both +1 and +2 node constructs. In lane 5, containing $H^{hex}N^{hex}A^{hex}$ + nodes 11, 12 , 14 and shown in purple, strong bands are seen at the +2 and + 3 node positions. Finally in lane 6, which contains $H^{hex}N^{hex}A^{hex}$ + nodes 11, 13, 14 and is shown in dark blue, has bands in the +1, +2 , and +3 node positions. The various combinations which could be causing the bands in each of these cases is given in Table 4.1. This table could be further refined by attaching the fluorophore selectively to certain nodes. This could provide further insight into which of the duplexes is stronger and the competition among the different constructs in the same lane.

Table 4.1: *Possible constructs in the bands observed in Figure 4.6. Given as (nodes) attached to* $H^{hex}N^{hex}$.

	Lane 4	Lane 5	Lane 6
	$H^{hex}N^{hex}$ + nodes (11, 14)	$H^{hex}N^{hex}$ + nodes (11, 12, 14)	$H^{hex}N^{hex}$ + nodes (11, 13, 14)
+3 nodes		(11, 12, 14)	(11, 13, 14)
+2 nodes	(11, 14)	(11, 12) or (11, 14)	(13, 14) or (11, 14)
+1 node	(11) or (14)		(11) or (14)

A similar step-wise build-up was then done for the $H^{hex}N^{hex}P^{hex}$ assembly and is shown in Figure 4.7. As with the previous gel, a Cy3 fluorophore was attached to the 2' position. The vertical intensity profiles for this gel are shown in Figure 4.8. While the full $H^{hex}N^{hex}P^{hex}$ construct assembles properly, several other features appear. The lanes 2, 3, and 5 which correspond to $H^{hex}N^{hex}$ + nodes (15), $H^{hex}N^{hex}$ + nodes (16), and $H^{hex}N^{hex}$ + nodes (12, 15) all contain bands in the +0 nodes ($H^{hex}N^{hex}$) position. This suggests that a significant portion of the new nodes did not stick in these cases. Addi-

tionally the +2 node band is completely missing in lane 5, meaning that none of the $H^{hex}N^{hex}$ + nodes (12, 15) construct formed. The various combinations for the bands observed in this gel are outlined in Table 4.2.

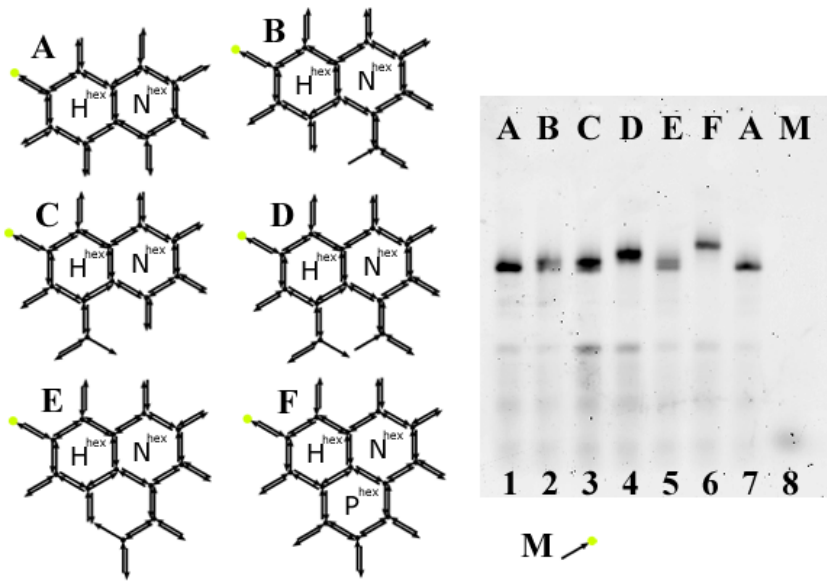

Figure 4.7: *The step-wise build-up of the $H^{hex}N^{hex}P^{hex}$ assembly.*

Table 4.2: *Possible constructs in the bands observed in Figure 4.8. Given as (nodes) attached to $H^{hex}N^{hex}$.*

	Lane 2	Lane 3	Lane 5
	$H^{hex}N^{hex}$ + nodes (15)	$H^{hex}N^{hex}$ + nodes (16)	$H^{hex}N^{hex}$ + nodes (12, 15)
+2 nodes			missing
+1 node	(5)	(16)	(15)
+0 nodes	()	()	()

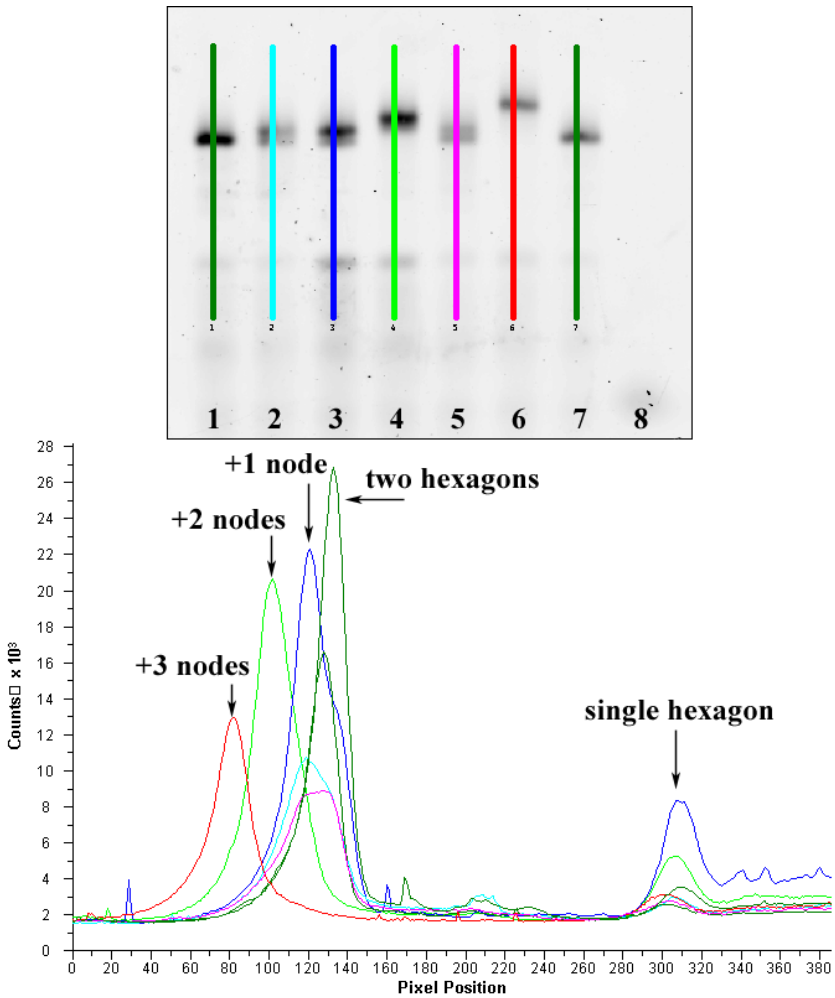

Figure 4.8: *An analysis of the constructs seen in the $H^{hex}N^{hex}P^{hex}$ assembly.*

In order to further investigate the strange bands observed in the $H^{hex}N^{hex}P^{hex}$ build-up further experiments were performed to confirm that the duplexes between nodes 1 and 16 as well as between nodes 10 and 15 do not form under certain conditions. Figure 4.9 shows a gel confirming that the intermediate struc-

tures do not form while the full $H^{hex}N^{hex}P^{hex}$ assembles properly. Lanes 1 and 5 contain $H^{hex}N^{hex}$ with Cy3 on the 2' position, which serve as a reference. Lanes 2, 3, and 4 contain intermediate structures with a ROX fluorophore attached on the node in question. Except for a faint band seen in lane 3 at the proper position for the $H^{hex}N^{hex}$ + nodes (12, 15) construct, the fluorophore containing monomers do not stick. Lane 6 contains $H^{hex}N^{hex}P^{hex}$ with Cy3 on the 2' position and serves as a reference for the next two lanes. Lanes 7 and 8 contain the $H^{hex}N^{hex}P^{hex}$ with ROX attached in the 16' and 12' positions respectively. These show that the full structure assembles properly. One possi-

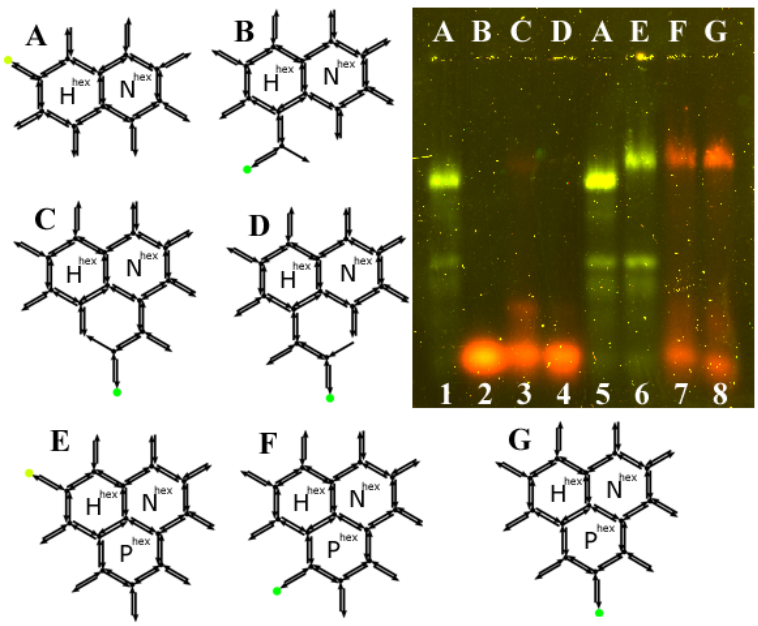

Figure 4.9: *A gel investigating the stability of several of the intermediate constructs in the $H^{hex}N^{hex}P^{hex}$ assembly.*

ble reason for the duplexes not forming could be interference from other oligos present in the mixture. In order to further investigate this possibility another gel, shown in Figure 4.10 was done to show if node 16 could stick to H^{hex} (lane

5). The left image shows the fluorophore scan while the right image shows the post staining with SybrGold to confirm that the structures formed. Since no construct band can be seen in lane 5, only monomers, it can be concluded that node 16 does not stick in this situation either. The exact reason for this remains under investigation. Shear forces ripping the new node off of the hexagon can be ruled out since the H^{hex} + node (7) construct, which is structurally identical, can be successfully formed [3]. The lack of a 'melting trail', which occurs when the monomer comes off during the gel electrophoresis, suggests that the node is not attached when the sample is placed into the gel. This rules out any possible effect during the gel, such as shear forces. The oligos which form the duplex in question were looked at with Mfold [20] in order to investigate the formation of secondary DNA structures such as hairpins, although this would be unlikely with a 10mer. This provided no hints as to the nature of the issue. The Gibb's free energy of the duplex was compared with other duplexes which are able to form intermediate products but this showed no discrepancies.

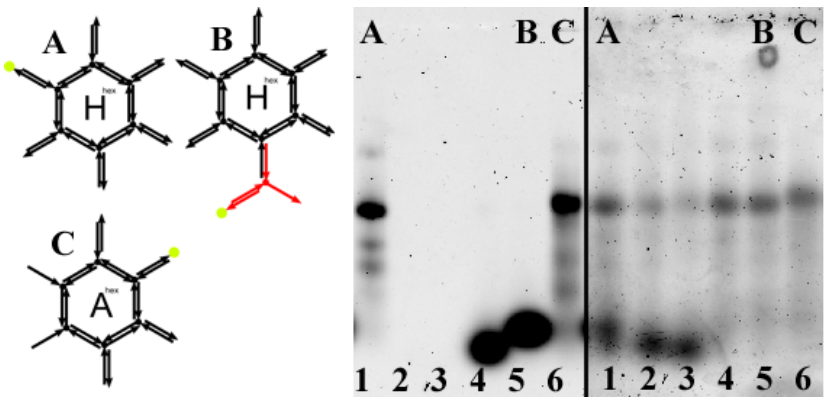

Figure 4.10: *A gel investigating how well node 16 can stick to node 1. The left side shows the laser fluorophore scan while the right side is stained with Sybr Gold to show all constructs. Node 16 did not stick to any construct despite the fact that all constructs assembled properly.*

Another possibility would be two arms on the node interacting with each

other. This was investigated for nodes 15 and 16 by first creating four fictitious 20mer sequences from the oligos which were anti-parallel with respect to the node, as shown in Figure 4.11. These were then analyzed in Mfold for possible secondary structures, using $[Na^+]$ = 200 mM. Three such structures, shown in Table 4.3, were found with a negative Gibb's free energy at room temperature. The hairpin structures predicted by Mfold in these cases are shown in Figure 4.12. Another factor to consider is that the timescale for the formation of the hairpins is likely to be be significantly smaller than that for the formation of duplexes with other nodes. The exact strength of competition between between secondary structures and the multi-node duplexes is still an open question, but it must be remembered that this simplistic analysis ignores the presence of the node between bases 10 and 11. Future analysis should take into account the presence of the node and how it affects the flexibility and separation of the oligo arms.

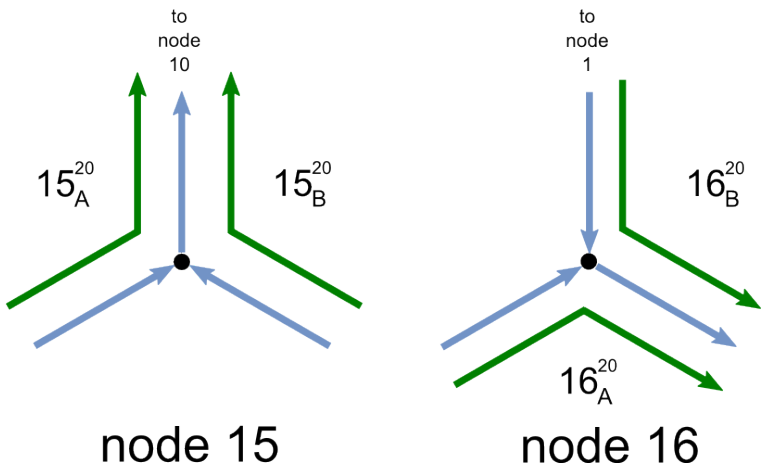

Figure 4.11: *The four fictitious 20mer oligos in nodes 15 and 16, created by taking appropriate combinations of anti-parallel oligos on the same node.*

Table 4.3: *The secondary structures possible in the four 20mer oligos in nodes 15 and 16.*

Name	Sequence (* indicates node position)	# BP	ΔG $\frac{kcal}{mol}$	T_M $^\circ C$	ΔH $\frac{kcal}{mol}$	ΔS $K \cdot mol$
15_A^{20}	CTACCTCGGA*GCCTTCATTG	2	-0.22	27	-20.9	-69.5
15_B^{20}	ACGAGTCCAG*GCCTTCATTG	-	-	-	-	-
16_A^{20}	AGTTGTCGCG*GACATGCGGA	4	-3.45	59	-32.4	-97.4
16_B^{20}	CCTCAAGCTG*GACATGCGGA	2	-0.02	24	-22.0	-73.9

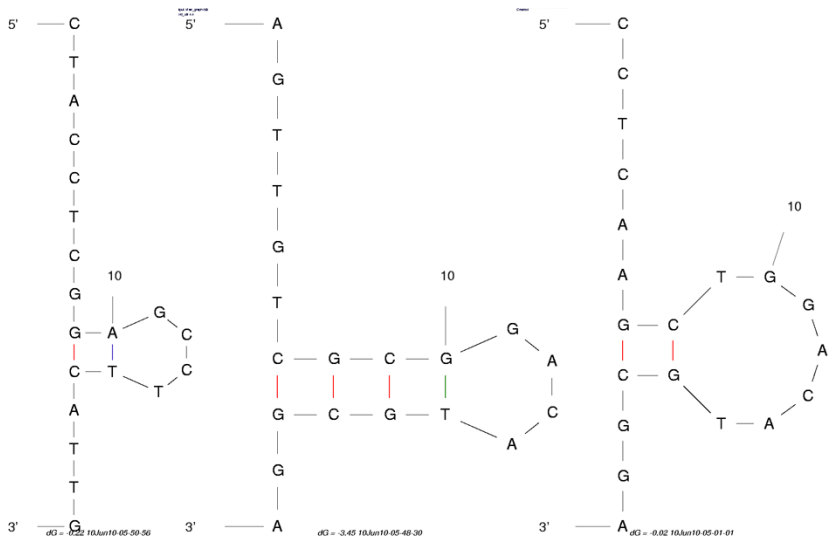

Figure 4.12: *The three secondary structures found through Mfold analysis. The structures correspond to the 15_A^{20}, 16_A^{20}, and 16_B^{20} oligos respectively from left to right. The position of the node is between bases 10 (labeled) and 11.*

4.1.3 Step-wise build-up of the Four Hexagon Assembly

Once the successful assembly of both the three hexagon structures had been confirmed a step-wise build-up was done for the final structure. Figure 4.13 shows the result of this gel. At this point in the project the DNA structure has become so large that the electrophoretic mobility is very low and distinguishing between the reference band (lane 1) and an intermediate structure with one extra node (lane 2) becomes difficult due to the small separation. Although the experiment was run for 5.5 hours, the separation between the three and four hexagon structures was approximately 1 mm. Nevertheless this gel as well as several repeats all showed a $H^{hex}N^{hex}A^{hex}P^{hex}$ band in a position appearing to confirm its assembly. One of the questions which the assembly of

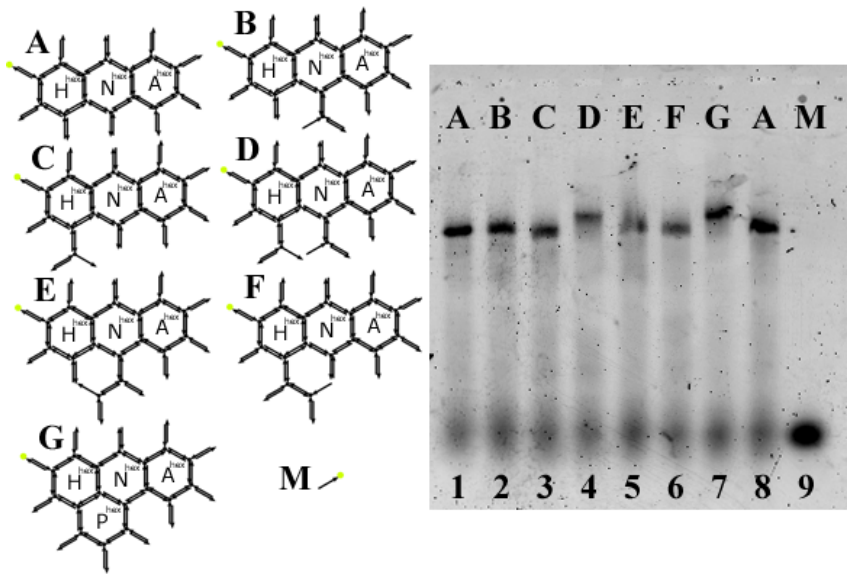

Figure 4.13: *The step-wise build-up of the $H^{hex}N^{hex}A^{hex}P^{hex}$ assembly.*

$H^{hex}N^{hex}A^{hex}P^{hex}$ sought to confirm was whether generic nodes, mentioned earlier, could be used. No evidence was seen that any interference between the two generic nodes occurred.

4.1.4 Assembly Yield

One important issue if the hexagonal grid is to be made even larger in the future, is the relationship between the yield and the number of hexagonal unit cells in the construct. Figure 4.14 shows all of the primary structures in this project from a single hexagon to all four, in the same gel. Since the assembled structures are individually labeled with fluorophores the molar ratio between the construct and the fluorophore is 1:1. This means that the intensity of the fluorophore signal is proportional to its concentration. This allows for the simple calculation of the yield of the hybridization, by comparing the intensity density of a single band to the total intensity density in the lane as shown in Figure 4.15. The plot shown in Figure 4.16 outlines the relationship between yield

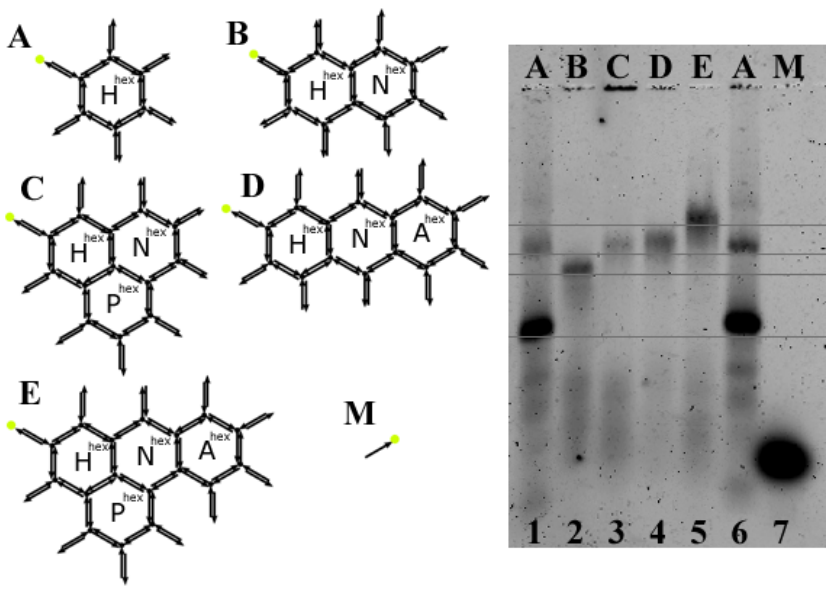

Figure 4.14: *The alternative structure assembled from the nodes for a single hexagon cell on the left. The 12 node assembly used to check for the alternative structure, on the right.*

and number of duplexes. Using the simplistic assumption that the yield of each

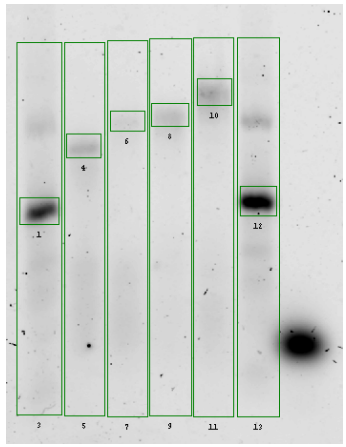

Figure 4.15: *Calculating the yield of the constructs in Figure 4.14.*

duplex formation in the structure is the same, a relationship governed by

$$Y_S = (Y_d)^{N_d} \tag{4.1}$$

can be fit to the data. Here Y_S is the yield of the structure, Y_d is the yield of every duplex, and N_d is the number of duplexes in the structure. Fitting this to the data gives a duplex formation yield of 94%. As expected the intermediate products have a lower yield than the whole hexagon assemblies. The yields for the constructs in Figure 4.14 is shown in Table 4.4.

Table 4.4: *The yields of various assemblies.*

Assembly	Yield (%)
$H^{hex}N^{hex}$	26
$H^{hex}N^{hex}P^{hex}$	20
$H^{hex}N^{hex}A^{hex}$	21
$H^{hex}N^{hex}A^{hex}P^{hex}$	16

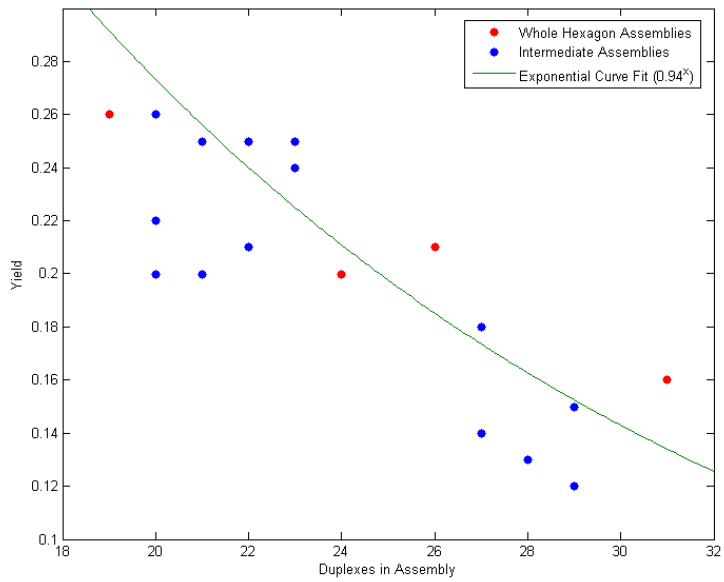

Figure 4.16: *A plot of the yield versus the number of duplexes in the structure. The red points correspond to whole hexagon structures while the blue points are intermediate assemblies with at least one unbound oligo arm.*

4.1.5 Alternative Structures

Several of the experiment performed demonstrated the formation of alternative structures. Figure 4.17 shows the most commonly observed alternative structure in the top right. This structure is seen when the single hexagon cell is assembled. It consists of 12 nodes, with two of each unique node present. Larger alternative structures could also occur with nodes in multiples of six. Additionally rings could theoretically interlock together, although the probability of this small. The bottom of Figure 4.17 shows a space-filling model of two rings interlocked.

In order to confirm the 12 node structure, a new reference assembly was created, which is shown on the left side of Figure 4.17. This consisted of the $H^{hex}N^{hex}P^{hex}$ structure which was missing its middle node (4). This created a large 12 node circular structure which should run at the same rate as the 12 node alternative structure in a gel. The result of this investigation is shown in Figure 4.18. Lane 1 contained the reference structure, while the highest band in lane 2 was the alternative structure which formed in a H^{hex} mixture. The stronger band in lane 2 a bit further down corresponds to the single hexagon. Lanes 3 through 8 also show a similar gel showing not only the 12 node alternative structure but the 18 node alternative structure as well. The yield of these alternative structure was calculated as 4.9% for the 12-node alternative structure, 2.4% for the 18-node alternative structure, compared to a yield of 26% for H^{hex}. It should be noted that this has been observed to fluctuate greatly from gel to gel. These formation of these structures should be examined as they reduce the yield of the desired product.

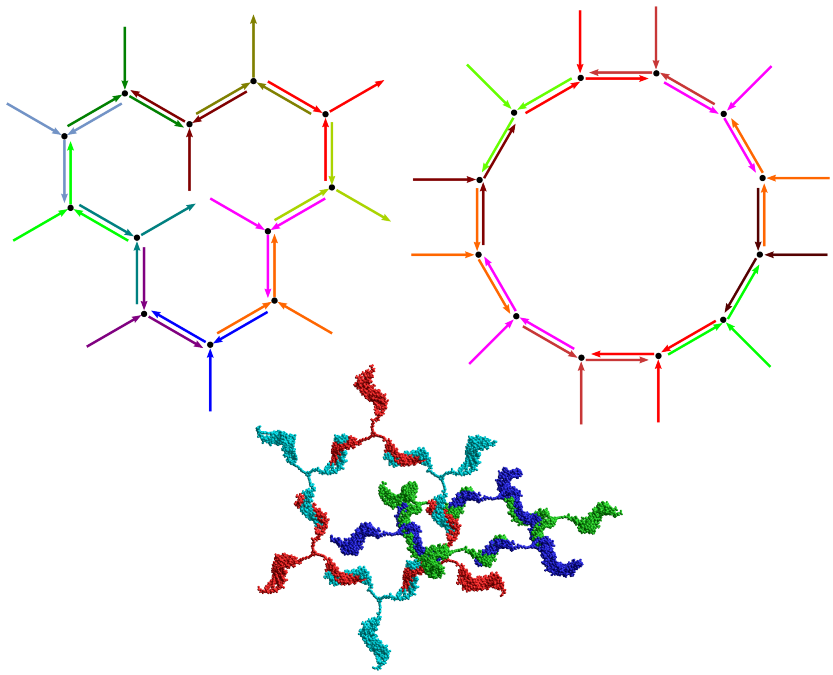

Figure 4.17: *The 12 node reference assembly used to check for the alternative structure, on the top left. The alternative structure assembled from the nodes for a single hexagon cell, on the top right. A space-filling model showing that rings could be joined together, on the bottom.*

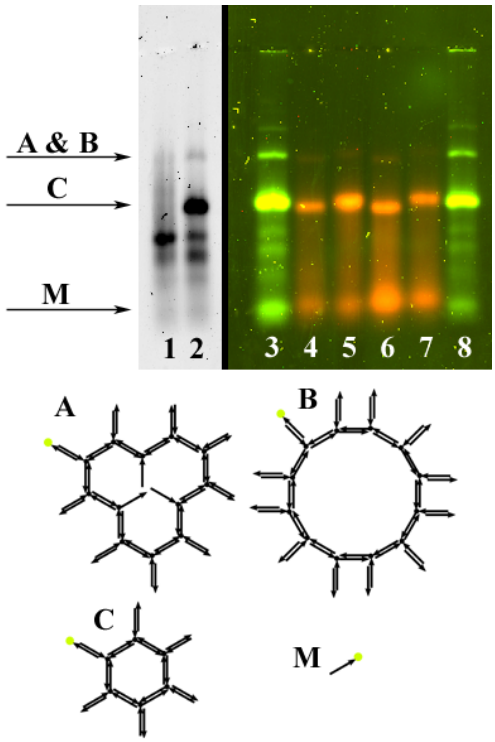

Figure 4.18: *Two gels showing some of the alternative structures seen.*

4.2 AFM

Due to the relative difficulty in using gel electrophoresis in characterizing large structures, as shown earlier, it is important to have a secondary method for verifying the structure formation. During the course of this project, the assembled structures were scanned with an AFM in the hopes of confirming the structure. Figure 4.19 shows the typical type of structure seen at the limits of resolution of the 1 μm scanner. Figure 4.20 shows a structure seen with the 100 μm scanner operating with the X-Y scanner in closed-loop mode. One of the challenges

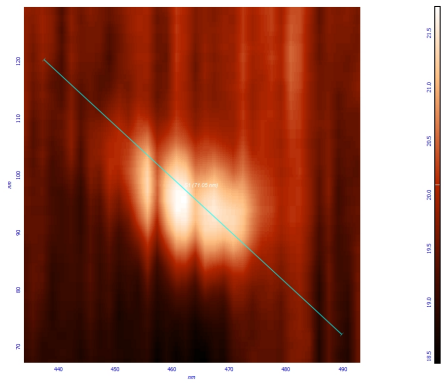

Figure 4.19: *A typical object seen at the limits of the resolution with the 1 μm scanner.*

with the 1 μm scanner was finding the optimum concentration of DNA so that there would be a high probability that a structure would be seen in a 1 by 1 μm area on the surface. A lower concentration would be used when working with the 100 μm scanner. Although objects were seen with a height of around 2 nm, as expected for DNA [21, 22], the finer geometry could not be made out in any of the samples measured.

One of the primary problems encountered was that once an object was seen with a large area scan, this object would disappear when a higher resolution scan was made at the objects position. It is possible that the tip would dislodge the structure on the first scan and change its position. Discussions with the AFM manufacturer, NT-MDT, resulted in the following recommendations for

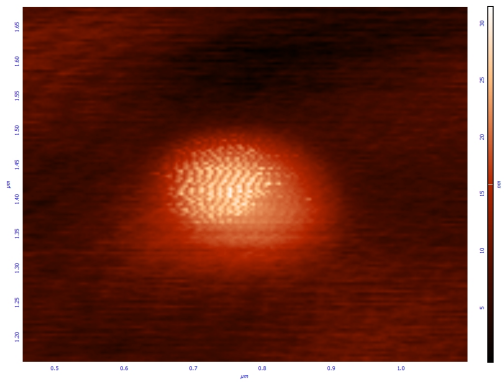

Figure 4.20: *A typical object seen with the 100 μm scanner.*

scanning:

- low amplitude (in the 10 nm range)
- scanning speed of 2 - 4 μm / sec in semi-contact mode
- turn on X-Y closed-loop feedback with the 100 μm scanner
- scan in an area less than 1 μm x 1 μm

Another possible issue is signal saturation. The gain of the AFM amplifies the signal from the Analog to Digital converter and improves the quality of the image. If the gradient of the amplified signal becomes larger than the scanning range of the Z scanner (about 10 μm) the signal will become saturated. This means that the inclination of the topography multiplied by the gain being used has to be less than 10 μm.

The AFM used in this project has a cover which can be placed over the entire scanner in order to isolate it from vibrations in the air and better control temperature and humidity. One interesting feature observed was that if the humidity changed, the features on the surface of the mica would also change. In general scans appeared to be better at higher humidities of about 35%. This could suggest distortions caused by surface charges. In order to combat this

effect the tip was grounded during the course of scans, which should aid in removing the charges from the surface. In one experiment, Nitrogen was pumped into the AFM chamber during scanning. This produced no noticable effect on the scans casting doubts on the surface charges being the source of problem.

Once it became clear that significant sources of error in the system would have to be reduced for proper imaging, various sources were examined individually. Problems with the systems could be split into two general areas: 1. factors affecting resolution and 2. contamination on the surface. In order to ensure proper operation of the system, several SPM calibration gratings were measured with the system. The TGZ1 grating from MicroMasch was used for vertical Z stage calibration as it has steps of 18.5 nm at a periodicity of 3 μm. The TDG01 grating had a periodicity of 278 nm with a height variation of 55 nm and was used to calibrate the X - Y stage. While testing showed no issues with the 1 μm scanner, Figure 4.21, the 100 μm scanner exhibited significant distortions as seen in Figure 4.22. The 100 μm scanner was placed through the re-calibration procedure as given by NT-MDT and subsequent scans no longer showed distortions, Figure 4.23. Scans with the larger 100 μm scanner often

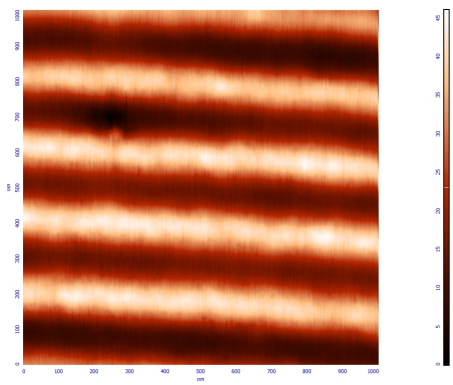

Figure 4.21: *A scan of the TDG01 calibration grating with the 1 μm scanner.*

showed large objects on the surface of the mica. An example of these can be seen in Figure 4.24. Several samples were also examined with the Veeco Di-

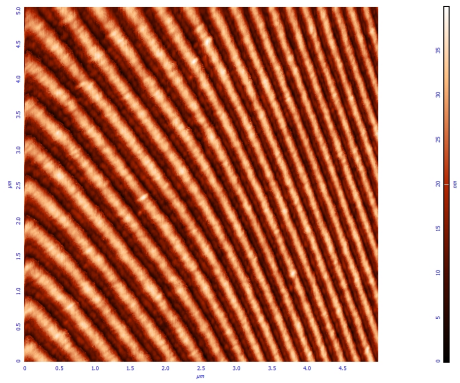

Figure 4.22: *A scan of the TDG01 calibration grating with the 100 μm scanner showing significant distortions.*

mension 3100 SPM in the Chalmers MC2 cleanroom. These also showed the same contamination on the surface, which suggests that the contamination is introduced during the sample preparation process. One suggestion put forward was that oil was present in the compressed air line. This should not apply for these samples as they were all cleaned with N_2 gas. Filtering the HEPES buffer and $NiCl_2$ solution though 0.2 μm filters did not remove the contaminants seen.

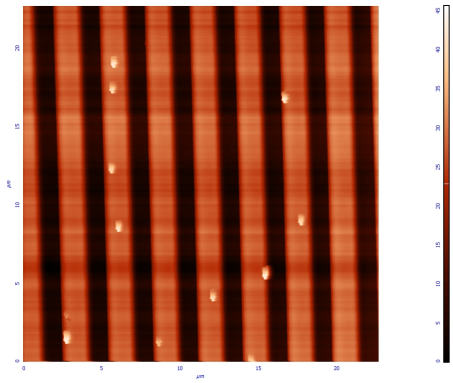

Figure 4.23: *A scan of the TGZ1 calibration grating after re-calibration of the 100 µm scanner no longer shows any distortions.*

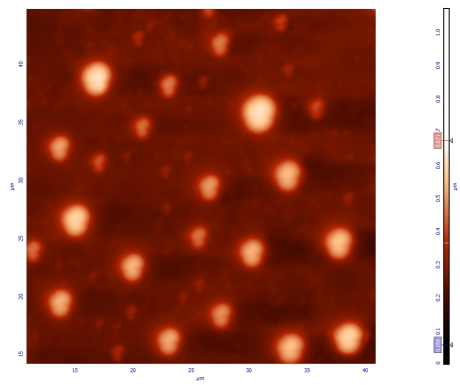

Figure 4.24: *Some of the contamination observed on many of the samples.*

5
Acknowledgments

I would like to thank my supervisor Erik Lundberg for his help and feedback during the course of this project. Thanks to Nima Hagshenas for helping me with the AFM system. Thank you to Bengt Nordén for allowing me to pursue my Master's thesis in his group. I am grateful to the Erasmus Mundus Master Nanoscience and Nanotechnology program for allowing me to pursue my Master's degree in Europe. Finally I would like to thank everyone in the Physical Chemistry for making this such a great place to do research.

Calin Plesa
Göteborg, June 2010

Bibliography

[1] R. Bruce Wallace, J. Shaffer, R.F. Murphy, J. Bonner, T. Hirose, and K. Itakura, "Hybridization of synthetic oligodeoxyribonucleotides to Phi X 174 DNA: the effect of single base pair mismatch," *Nucleic Acids Research*, vol. 6, no. 11, pp. 3543–3558, April 1979.

[2] Jr. John SantaLucia, "A unified view of polymer, dumbbell, and oligonucleotide DNA nearest-neighbor thermodynamics," *PNAS*, vol. 95, no. 4, pp. 1460–1465, February 1998.

[3] J. Tumpane, R. Kumar, E.P. Lundberg, P. Sandin, N. Gale, I.S. Nandhakumar, B. Albinsson, P. Lincoln, L.M. Wilhelmsson, T. Brown, et al., "Triplex addressability as a basis for functional DNA nanostructures," *Nano Lett*, vol. 7, no. 12, pp. 3832–3839, 2007.

[4] J. Chen and N.C. Seeman, "Synthesis from DNA of a molecule with the connectivity of a cube," 1991.

[5] H. Bugl, J.P. Danner, R.J. Molinari, J.T. Mulligan, H.O. Park, B. Reichert, D.A. Roth, R. Wagner, B. Budowle, R.M. Scripp, et al., "DNA synthesis and biological security," *Nature Biotechnology*, vol. 25, no. 6, pp. 627–629, 2007.

[6] P.W.K. Rothemund, "Folding DNA to create nanoscale shapes and patterns," *Nature*, vol. 440, no. 7082, pp. 297–302, 2006.

[7] R.J. Kershner, L.D. Bozano, C.M. Micheel, A.M. Hung, A.R. Fornof, J.N. Cha, C.T. Rettner, M. Bersani, J. Frommer, P.W.K. Rothemund, et al., "Placement and orientation of individual DNA shapes on lithographically patterned surfaces," *Nature Nanotechnology*, vol. 4, no. 9, pp. 557–561, 2009.

[8] E.S. Andersen, M. Dong, M.M. Nielsen, K. Jahn, R. Subramani, W. Mamdouh, M.M. Golas, B. Sander, H. Stark, C.L.P. Oliveira, et al., "Self-assembly of a

nanoscale DNA box with a controllable lid," *Nature*, vol. 459, no. 7243, pp. 73–76, 2009.

[9] AG Ogston, "The spaces in a uniform random suspension of fibres," *Transactions of the Faraday Society*, vol. 54, pp. 1754–1757, 1958.

[10] D. Rodbard and A. Chrambach, "Unified theory for gel electrophoresis and gel filtration," *Proceedings of the National Academy of Sciences of the United States of America*, vol. 65, no. 4, pp. 970, 1970.

[11] G.W. Slater, J. Rousseau, J. Noolandi, C. Turmel, and M. Lalande, "Quantitative analysis of the three regimes of DNA electrophoresis in agarose gels," *Biopolymers*, vol. 27, no. 3, pp. 509–524, 2004.

[12] SP Timoshenko and JN Goodier, *In:(3rd edn. ed.), Theory of Elasticity*, McGraw-Hill, New York, 1970.

[13] M.A. Poggi, A.W. McFarland, J.S. Colton, and L.A. Bottomley, "A method for calculating the spring constant of atomic force microscopy cantilevers with a non-rectangular cross section," *Anal. Chem*, vol. 77, no. 4, pp. 1192–1195, 2005.

[14] J. Tumpane, P. Sandin, R. Kumar, V.E.C. Powers, E.P. Lundberg, N. Gale, P. Baglioni, J.M. Lehn, B. Albinsson, P. Lincoln, et al., "Addressable high-information-density DNA nanostructures," *Chemical Physics Letters*, vol. 440, no. 1-3, pp. 125–129, 2007.

[15] E.P. Lundberg, A.H. El-Sagheer, P. Kocalka, L.M. Wilhelmsson, T. Brown, and B. Nordén, "A new fixation strategy for addressable nano-network building blocks," *Chemical Communications*, 2010.

[16] E.P. Lundberg, A.H. El-Sagheer, P. Kocalka, M.L. Wilhelmsson, T. Brown, and B. Nordén, "Fixation of Self-Assembled DNA Nanostructures by Simultaneous Multicenter Click Chemistry," *Biophysical Journal*, vol. 98, pp. 658, 2010.

[17] M. Bezanilla, S. Manne, D.E. Laney, Y.L. Lyubchenko, and H.G. Hansma, "Adsorption of DNA to mica, silylated mica, and minerals: characterization by atomic force microscopy," *Langmuir*, vol. 11, no. 2, pp. 655–659, 1995.

[18] H G Hansma and D E Laney, "DNA binding to mica correlates with cationic radius: assay by atomic force microscopy," *Biophysical Journal*, vol. 70, no. 4, pp. 1933–1939, April 1996.

[19] D. Pastré, O. Piétrement, S. Fusil, F. Landousy, J. Jeusset, M.O. David, L. Hamon, E. Le Cam, and A. Zozime, "Adsorption of DNA to mica mediated by divalent

counterions: a theoretical and experimental study," *Biophysical journal*, vol. 85, no. 4, pp. 2507–2518, 2003.

[20] M. Zuker, "Mfold web server for nucleic acid folding and hybridization prediction," *Nucleic acids research*, vol. 31, no. 13, pp. 3406, 2003.

[21] J. Vesenka, T. Marsh, E. Henderson, and C. Vellandi, "The diameter of duplex and quadruplex DNA measured by Scanning Probe Microscopy," *press, Scanning Microscopy*, 1997.

[22] T. Muir, E. Morales, J. Root, I. Kumar, B. Garcia, C. Vellandi, D. Jenigian, T. Marsh, E. Henderson, and J. Vesenka, "The morphology of duplex and quadruplex DNA on mica," *Journal of Vacuum Science & Technology A: Vacuum, Surfaces, and Films*, vol. 16, pp. 1172, 1998.

6

Appendix

6.1 Phosphate Buffer

The following Phosphate Buffer recipe was used throughout this project.

Phosphate Buffer 109mM	
$[pH]$	7.5
$[Phosphate]$	109 mM
$[Na^{+}]$	200 mM
$H_2NaO_4PH_2O$	137.99 g/mol 2.399 g
$Na_2HPO_42H_20$	177.99 g/mol 16.247 g
$MilliQ$	1000 mL

6.2 AFM procedure

1. Mount scanner and connect to base
2. Mount head and connect to base
3. Mount tip and connect to head
4. Turn on TableStable
5. Launch configurator with options: Universal Base Unit, Vacuum exch. mount, 1 μm scanner, Universal SPM head, Adjustment unit for Spreading Resistance Measurements
6. Use z01057y.par for 1 μm scanner
7. Update configuration and launch Nova
8. Turn on SPM controller
9. Allow AFM to warm up for 30 min while preparing sample
10. Check relative humidity
11. Mount sample and connect ground wire
12. Manually lower tip and place hood on
13. Find probe's resonance (130 kHz)
14. Approach tip to sample, wait for Approach Done message
15. Turn off Auto Set Point and manually set set point to 0.8 x Mag
16. Turn feedback on/off to check for tip contact
17. Look at Force curves
18. Begin scanning
19. If the relative humidity begins to increase, the set point must be lowered